



Using PFISR measurements and gravity wave dissipative theory to determine the neutral, background thermospheric winds

Sharon L. Vadas¹ and Michael J. Nicolls²

Received 30 July 2007; revised 8 November 2007; accepted 20 November 2007; published 18 January 2008.

[1] Understanding the propagation and dissipation of an atmospheric gravity wave (GW) in the thermosphere requires an accurate dissipative GW dispersion relation, the GW's horizontal wavelength and period, and the background neutral winds and temperatures. Conversely, if the GW's horizontal wavelength, period, and vertically-varying vertical wavelengths are known instead along with the background temperatures, then the background, horizontal neutral winds along the GW propagation direction can be calculated using GW dissipative theory. Recent daytime observations using the Advanced Modular Incoherent Scatter Radar (AMISR) located in Poker Flat, Alaska, the Poker Flat Incoherent Scatter Radar (PFISR), have obtained these latter parameters. Using PFISR data for a GW on December 13, 2006, we calculate the average, background, horizontal neutral winds at $z \sim 160\text{--}240$ km. **Citation:** Vadas, S. L., and M. J. Nicolls (2008), Using PFISR measurements and gravity wave dissipative theory to determine the neutral, background thermospheric winds, *Geophys. Res. Lett.*, 35, L02105, doi:10.1029/2007GL031522.

1. Introduction

[2] Gravity waves (GWs) are created when neutral, stable fluid is disturbed. In the ionosphere, propagating neutral GWs push and pull plasma along the Earth's magnetic field lines, which causes periodic advection and compression of the plasma called traveling ionospheric disturbances (TIDs) [e.g., *Hocke and Schlegel*, 1996]. Because the density decreases nearly exponentially with altitude z , GW amplitudes grow nearly exponentially with z prior to dissipation. The most important sources of thermospheric dissipation for high-frequency, large vertical wavelength GWs are kinematic viscosity (ν) and thermal diffusivity (\mathcal{K}) [*Vadas and Fritts*, 2005] (hereinafter referred to as VF2005). *Pitteway and Hines* [1963] derived the first GW dissipative dispersion relations that included ν and \mathcal{K} by assuming the vertical wavenumber m to be complex, implying explicit GW damping with altitude. One of these dispersion relations was used to show how the vertical tilting of TIDs with altitude observed by *Thome* [1964] could be explained as a GW dissipating [*Hines*, 1968], since this dispersion relation predicts that a GW's vertical wavelength $\lambda_z = 2\pi/m$ increases to infinity while dissipating. However, this solution has several problems. The first is that

the dissipative effects of ν and \mathcal{K} were treated separately, yielding different GW dispersion relations and amplitude formulas. In fact, the possible unphysical growth of a GW's amplitude with altitude for $z \rightarrow \infty$ using the dispersion relation for ν only led *Hines* [1968] to utilize the dispersion relation for \mathcal{K} only. The second and more serious problem is that these dispersion relations were derived by applying a perturbation expansion to lowest order in ν or \mathcal{K} to the complex GW solutions. Thus, these dispersion relations are only valid where dissipation is weak, and thus cannot accurately predict the changes in λ_z which occur during strong dissipation.

[3] Recently, VF2005 derived a more complete GW anelastic dispersion relation that includes ν and \mathcal{K} , and is accurate during strong dissipation. This dispersion relation reduces to the Boissinesq solution in the appropriate limit. However, λ_z may increase or decrease with z during dissipation, depending on the temperature and horizontal winds.

[4] With this new dispersion relation, a wealth of information can be unlocked from observations of individually-propagating GWs if enough GW parameters are measured. Recent PFISR observations are ideal, because GW horizontal and vertical wavelengths and periods are measured. The purpose of this paper is to calculate the average, neutral, horizontal, background thermospheric winds using a single GW observed by PFISR and GW dissipative theory.

2. GW Dissipative Theory

[5] VF2005 derived a GW anelastic dispersion relation which is accurate during strong dissipation in the thermosphere. This dispersion relation assumes that ion drag can be neglected, which is a good assumption for GWs with periods less than a few hours [*Hines and Hooke*, 1970]. This is the exact solution for a high-frequency GW with phase speed much less than the speed of sound, and which propagates through an atmosphere with constant temperature, wind, viscosity coefficient μ , and Prandtl number Pr . Additionally, this GW must have $\lambda_z \ll 4\pi H$ during strong dissipation for the kinematic viscosity, $\nu = \mu/\bar{\rho}$, to be locally constant, where H is the density scale height and $\bar{\rho}$ is the mean density. After redefining the fluid variables to scale out $\bar{\rho}$, VF2005 postulated that the GW solution from a temporally-localized source can be written as decaying explicitly in time and implicitly in altitude. This is equivalent to setting the wave frequency, rather than $m = 2\pi/\lambda_z$, complex. This yields a complex dispersion relation which is analytically separable into a GW dispersion relation and the amplitude decay with time, unlike the inseparable complex

¹CoRA Division, NorthWest Research Associates, Boulder, Colorado, USA.

²SRI International, Menlo Park, California, USA.

equation one obtains if m is assumed complex instead. This dispersion relation is

$$\omega_{Ir}^2 = \frac{k_H^2 N^2}{(\mathbf{k}^2 + 1/4H^2)(1 + \delta_+ + \delta^2/\text{Pr})} \left[1 + \frac{\nu^2}{4\omega_{Ir}^2} \left(\mathbf{k}^2 - \frac{1}{4H^2} \right)^2 \frac{(1 - \text{Pr}^{-1})^2}{(1 + \delta_+/2)^2} \right]^{-1}, \quad (1)$$

where $\mathbf{k} = (k, l, m)$ is the GW zonal, meridional, and vertical wavenumber components in geographic coordinates, respectively, ($\lambda_x = 2\pi/k$, $\lambda_y = 2\pi/l$, $\lambda_z = 2\pi/m$) is the wavelength vector, $k_H^2 = k^2 + l^2$, $\mathbf{k}^2 = k_H^2 + m^2$, N is the buoyancy frequency, $\delta = \nu m/H\omega_{Ir}$, $\delta_+ = \delta(1 + \text{Pr}^{-1})$, $\omega_{Ir} = \omega_r - kU - lV$ or

$$\omega_{Ir} = \omega_r - k_H U_H \quad (2)$$

is the intrinsic GW frequency, ω_r is the ground-based (i.e., observed) GW frequency, U and V are the background neutral zonal and meridional winds, respectively, and $U_H = (kU + lV)/k_H$ is the background, neutral wind along the direction of GW propagation. U and V may include components from large-scale waves and tides, GW dissipation, and ion drag on the neutrals from ions accelerated from geomagnetic storms. The neutral wind perpendicular to a GW's propagation direction does not affect its propagation. If the neutral wind vector changes direction with altitude, $\lambda_H = 2\pi/k_H$ is constant if U and V are independent of x and y . Additionally, assuming negligible reflection from viscosity, a GW's amplitude grows in altitude as $\propto 1/\sqrt{\rho}$, but decays from dissipation as $\exp(\omega_{Ir}t)$, where (VF2005)

$$\omega_{Ir} = -\frac{\nu}{2} \left(\mathbf{k}^2 - \frac{1}{4H^2} \right) \frac{[1 + (1 + 2\delta)/\text{Pr}]}{(1 + \delta_+/2)}. \quad (3)$$

The ray-trace code which utilizes these expressions is described by *Vadas* [2007]. Although $\lambda_z(z)$ or $U_H(z)$ can be determined using equation (1), ray-tracing is necessary to determine a GW's amplitude as a function of altitude and/or time via equation (3).

[6] One important assumption used to derive these expressions is that the background wind shears are not too large:

$$|\lambda_z| < 2\pi|U_H/(dU_H/dz)|. \quad (4)$$

A typical F region GW with $\lambda_z \simeq 100\text{--}300$ km [e.g., *Djuth et al.*, 1997] will refract according to equation (1) if $dU_H/dz < U_H$ (0.02–0.06) m/s/km, which is $dU_H/dz < (4\text{--}12)$ m/s/km for $U_H \simeq 200$ m/s. A GW's λ_z likely only reflects the actual wind if equation (4) is satisfied everywhere in the thermosphere; otherwise, λ_z likely reflects the average wind. However, because of strong viscous damping, it is possible that very large neutral vertical wind shears cannot be maintained in the thermosphere. Note that λ_z can be much larger than the shear depth because $\lambda_z/2\pi = m^{-1}$, not λ_z , must be smaller than the depth of the shear from equation (4).

3. The PFISR Measurements of GWs

[7] As described in detail by *Nicolls and Heinselman* [2007], the 96-panel AMISR system, the PFISR, is located

at the Poker Flat Research Range (65.13°N, 147.47°W) near Fairbanks, Alaska. AMISR technology allows the experimenter to steer the beam on a pulse-to-pulse basis using phased array techniques, thereby pointing essentially simultaneously at multiple positions in the sky. Since PFISR began operations in late 2006, clearly identifiable wave signatures have been observed in many datasets taken during the daytime (when there is significant F-region ionization and the wave signatures can be distinguished from auroral effects), with varying periods and wavelengths.

[8] *Nicolls and Heinselman* [2007] report on recent PFISR observations of GWs made on December 13, 2006. Figure 1 shows the measured electron densities, N_e , the relative electron density perturbations, $\delta N_e/N_e = (N_e - \bar{N}_e)/\bar{N}_e$, the line-of-sight (*los*) ion velocities, V_{los} , and the filtered V_{los} . The background electron density, \bar{N}_e , is computed via low pass filtering on a beam-by-beam basis which removes waves with periods less than ~ 35 minutes. The filtered V_{los} perturbations are computed by applying a band-pass filter to V_{los} to remove waves with periods less than ~ 10 min and greater than ~ 35 min. The banded structures clearly indicate the presence of GWs, with downward moving phases indicating upward-propagating GWs. One GW is present at 21:00–22:00 UT, while another is present at 22:00–23:30 UT. Local standard time is LST = UT-9. The slopes of the GW phases change with altitude, indicating changes of λ_z with altitude, since the GW phase is proportional to $\exp(i \int m dz)$. For the GW from 22:00–23:30 UT, the relative electron density perturbations are largest at $z \sim 180\text{--}200$ km, while V_{los} peaks at higher altitudes, $z \sim 220$ km. Additionally, V_{los} lags in phase by 90° behind $\delta N_e/N_e$. This phase lag, and the result that the ion density and V_{los} peak at different altitudes, follows from the ion continuity equation (S. L. Vadas and M. J. Nicolls, Temporal evolution of neutral, thermospheric winds and plasma response, manuscript in preparation, 2007, hereinafter referred to as Vadas and Nicolls, manuscript in preparation, 2007). Note that V_{los} are small, 10–20 m/s, indicative of low geomagnetic activity. The plasma oscillations are induced by the GW via neutral-ion collisions. Because the ions are confined to move along the magnetic field line, the V_{los} perturbation (i.e., the oscillatory component of V_{los}) approximately equals the GW vertical velocity, w' , since the magnetic field is nearly vertical at Poker Flat (PF), with a dip angle $I = 77^\circ$. We therefore estimate $w' \sim 15$ m/s for this GW at $z \sim 220$ km.

[9] Using $\delta N_e/N_e$, *Nicolls and Heinselman* [2007] determined that the GW from 22:00–23:30 UT had $\lambda_x = 373 \pm 28$ km, $\lambda_y = -216 \pm 12$ km, $\lambda_H = 187 \pm 8$ km, and a ground-based period of $\tau_r = 22.3 \pm 1.1$ min. The GW's ground-based horizontal phase speed was $c_H = \omega_r/k_H = \lambda_H/\tau_r \sim 140$ m/s. Vertical profiles of λ_x and λ_y are shown in Figure 2a, along with the propagation angle counterclockwise from east, $\theta = \tan^{-1}(\lambda_x/\lambda_y)$. This GW was propagating $\sim 30^\circ$ east of south. Since this GW has a period much less than a few hours, its amplitude and dispersion are likely unaffected by ion drag. Figure 2b shows the measured λ_z profile, calculated from the averaged phase slopes of $\delta N_e/N_e$ from the 2 wave pulses between $\sim 22:00\text{--}22:50$ UT from the vertically-pointed beam. $|\lambda_z|$ increases rapidly from $\lambda_z \sim -150$ km

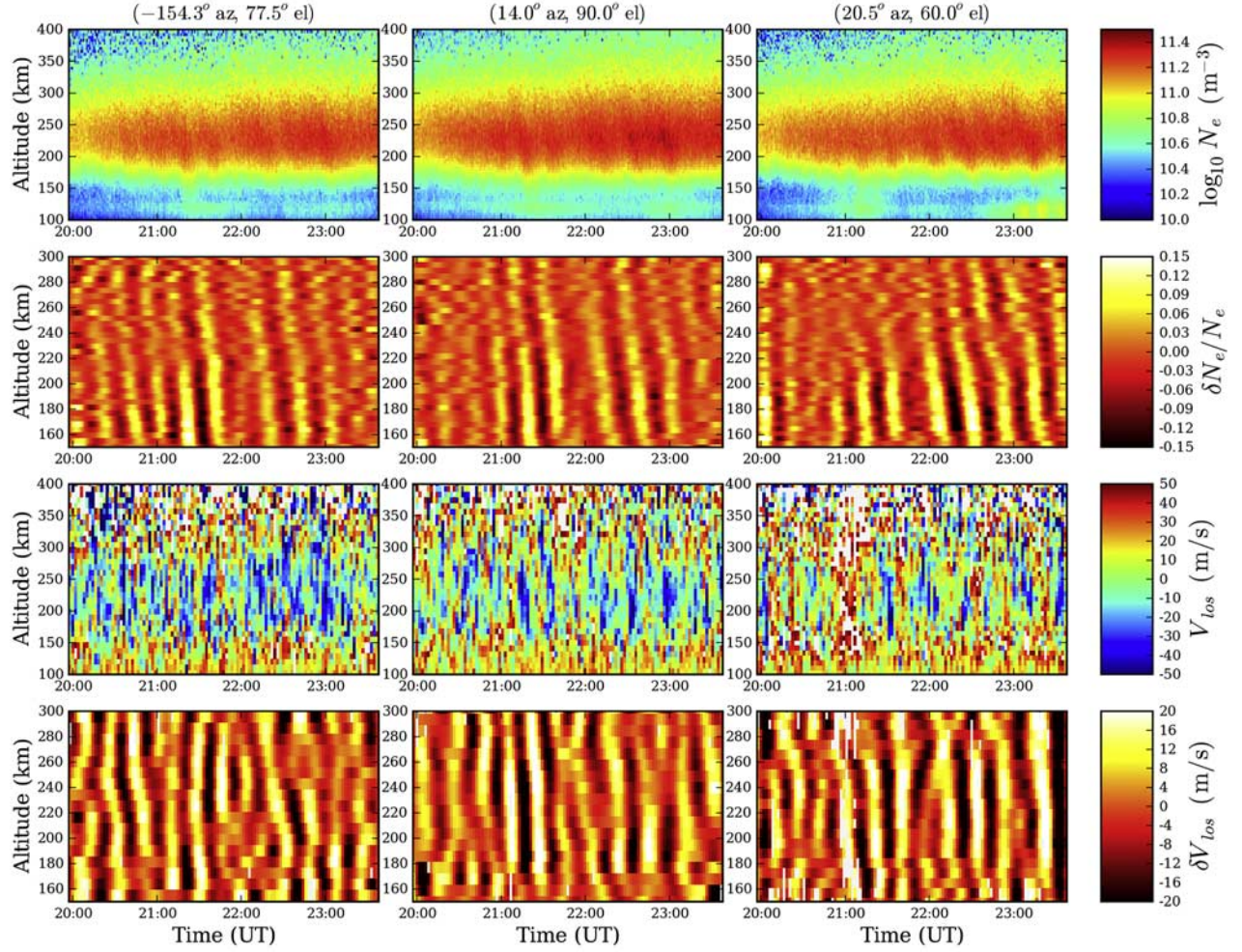


Figure 1. Measured quantities for 3 of the 10 beams. Electron densities, N_e , (first row). Band pass filtered relative electron density perturbations, $\delta N_e/N_e$, (second row). Line-of-sight ion velocities, V_{los} , (third row). Band-pass filtered V_{los} perturbations (forth row). The left column is up the B-field line, the middle column indicates the vertically-pointed beam, and the right column indicates a third beam. Similar oscillations were observed in all beams [Nicolls and Heinselman, 2007].

at $z = 160$ km, peaks at $z = 190$ km with $\lambda_z \sim -400$ km, and decreases rapidly for higher altitudes to $\lambda_z \sim -200$ km.

4. GW Propagation and Dissipation

[10] Using the MSIS temperature \bar{T} shown in Figure 2c from the NRLMSISE-00 model [Hedin, 1991], $\text{Pr} = 0.7$, and $\mu = 3.34 \times 10^{-4} \bar{T}^{0.71} \text{ gm m}^{-1} \text{ s}^{-1}$, we ray-traced the GW observed by PFISR through zero winds. λ_z is shown in Figure 2b. Since $|\lambda_z|$ is much smaller than the measured values, the background winds must have been strong and opposite to the GW's propagation direction. We also ray-trace this GW through a northward wind of 200 m/s shown in Figure 2c, which has a projection along the GW propagation direction of $V \sin(\theta) \sim -170$ m/s. λ_z is shown in Figure 2b. Here, $|\lambda_z|$ increases to much larger values than for zero wind, consistent with the data for $z \sim 160$ km and $z \sim 210$ –230 km; however, $|\lambda_z|$ significantly underestimates the data for $z \sim 170$ –200 km.

[11] Although the ray-trace λ_z curves in Figure 2b could have been computed from equation (1), the GW amplitudes can only be determined via ray-tracing. We show in

Figure 2b the altitudes where the ray-traced GW momentum fluxes, $u'w'$, are maximum, z_{diss} , as a square and triangle for the zero wind and northward wind, respectively. Comparing with Figure 1, $\delta N_e/N_e$ maximizes at a lower altitude than z_{diss} . This occurs because the electron density perturbation does not peak where the GW amplitude peaks; rather, the ion density responds most strongly to rapid changes with altitude in the background electron density and/or the GW amplitude. Additionally, the GW's ray-traced vertical velocity, w' , peaks at $z \sim 225$ km, consistent with the peak altitude for V_{los} along the B-field direction (Vadas and Nicolls, manuscript in preparation, 2007). Since the rapid changes in λ_z occur well below z_{diss} , these changes are due to background wind variations rather than dissipation.

[12] Using the $\lambda_z(z)$ data from Figure 2b, we solve equation (1) iteratively for $\omega_{I_r}(z)$ starting at the lowest altitude where ν is negligible, and using ω_{I_r} solutions as initial guesses as z is increased. Figure 2d shows this GW's vertically-varying intrinsic wave period, $\tau_{I_r} = 2\pi/\omega_{I_r}$, and the buoyancy period, $2\pi/N$. Note that $\tau_{I_r} \sim 11$ min at $z \sim 160$ km, decreases to 8 min at $z \sim 190$ km, and increases to 11 min at $z \sim 220$ km. Although τ_{I_r} is close to

the buoyancy period at $z \sim 190$ km, $\tau_{Ir}(z) > 2\pi/N$. If $\tau_{Ir} = 2\pi/N$, an upward-propagating GW reflects downward.

5. Neutral Wind Along GW Direction

[13] Because ω_r and λ_H are constant with altitude, the variation of ω_{Ir} with altitude is due to neutral, background

winds. Using equation (2), the neutral, average background wind projected along the direction of GW propagation is

$$U_H(z) = \lambda_H \left(\frac{1}{\tau_r} - \frac{1}{\tau_{Ir}} \right). \quad (5)$$

Using $\tau_{Ir}(z)$ from Figure 2d, we show $U_H(z)$ in Figure 2e. Note that the angle of U_H counterclockwise from east is θ . As expected, the neutral wind projection is opposite to the GW propagation direction. Although the calculated winds are -160 m/s at $z \sim 160$ km and $z \geq 220$ km, consistent with tidal amplitudes, they are much larger at $z \sim 190$ km: $U_H \sim -250$ m/s. This rapid increase and decrease over a vertical depth of 40 km likely is not due to thermospheric tides, because tidal amplitudes are viscously-limited above $z \sim 150$ km [e.g., *Roble, 1995*]. Note that $\lambda_z/2\pi < 65$ km, which implies that the extracted, average winds are marginally resolved by this GW vertically-varying parameters.

[14] These extracted winds, U_H , are somewhat sensitive to \bar{T} . An increase in \bar{T} by 20% causes a decrease in N of $\sim 10\%$ and an increase in H of $\sim 20\%$, using the isothermal expressions $N^2 \propto \bar{T}^{-1}$ and $H \propto \bar{T}$ [e.g., *Vadas and Fritts, 2006*]. We ignore H for this GW because $k_H^2 \gg 1/4H^2$ and $\delta \sim 0$ at $z < 210$ km. A decrease in N by $\sim 10\%$ causes a decrease in ω_{Ir} by $\sim 10\%$ from equation (1), which causes a $\pm 10\omega_{Ir}/k_H|U_H| \sim \pm 15\%$ increase/decrease in $|U_H|$ from equation (2), depending on the sign of U_H . Since $U_H < 0$, a 20% decrease (increase) of \bar{T} to 650 and 1000 K results in a 15% increase (decrease) of the extracted neutral wind at $z \sim 180$ km by ~ 40 m/s for this GW.

6. Total Neutral Thermospheric Wind

[15] V_{los} consists of oscillatory and mean components. Figure 3a shows the mean component of V_{los} , defined as V_{ap} , obtained by averaging V_{los} along the B-field direction for 1 hour from 22–23 UT. At PF, the declination angle is 22° east of north. This approximately constant plasma motion results from a combination of 1) ion diffusion and 2) ion drag acting on the component of the background neutral wind along the magnetic meridian, and has often been used to infer the neutral winds along the magnetic meridian with ISR measurements [e.g., *Buonsanto and Witasse, 1999; Aponte et al., 2005*]. Neglecting diffusion, the background, horizontal, neutral wind along the magnetic meridian is $U_m \sim -V_{ap}/\cos(I)$. We overlay U_m in Figure 3a.

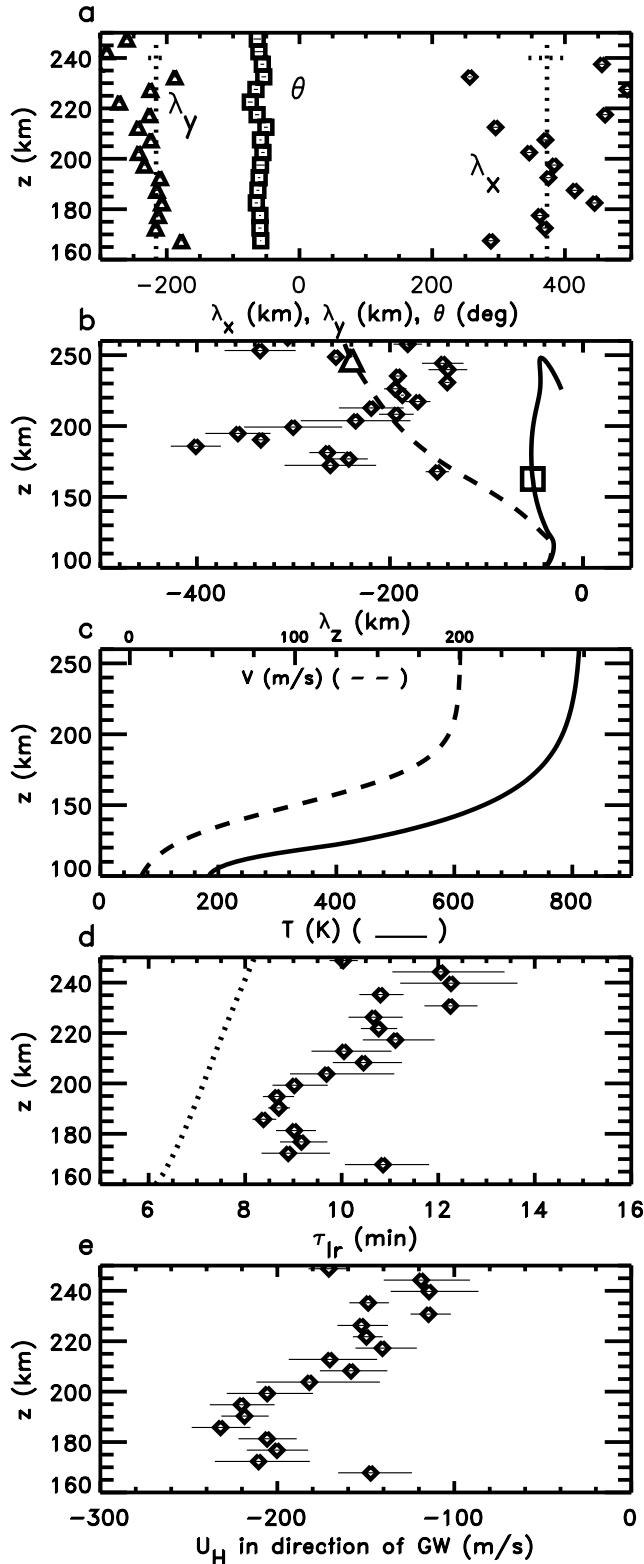


Figure 2. (a) λ_x (diamonds), λ_y (triangles), and angle of propagation, θ , (squares). Vertical dotted lines show $\lambda_x = 373$ km and $\lambda_y = -216$ km, while horizontal dotted lines show the combined errors, $\Delta\lambda_x = 28$ km and $\Delta\lambda_y = 12$ km. (b) λ_z (diamonds). Ray-traced λ_z through zero wind (solid line) and the northward wind shown in Figure 2c (dashed line). (c) MSIS \bar{T} (solid line, lower x-axis), and idealized northward wind (dashed line, upper x-axis). (d) $\tau_{Ir} = 2\pi/\omega_{Ir}$ computed from equation (1) (diamonds). Dotted line shows $2\pi/N$. (e) $U_H(z)$, calculated from equation (5) (diamonds). Errors are shown as solid, horizontal lines.

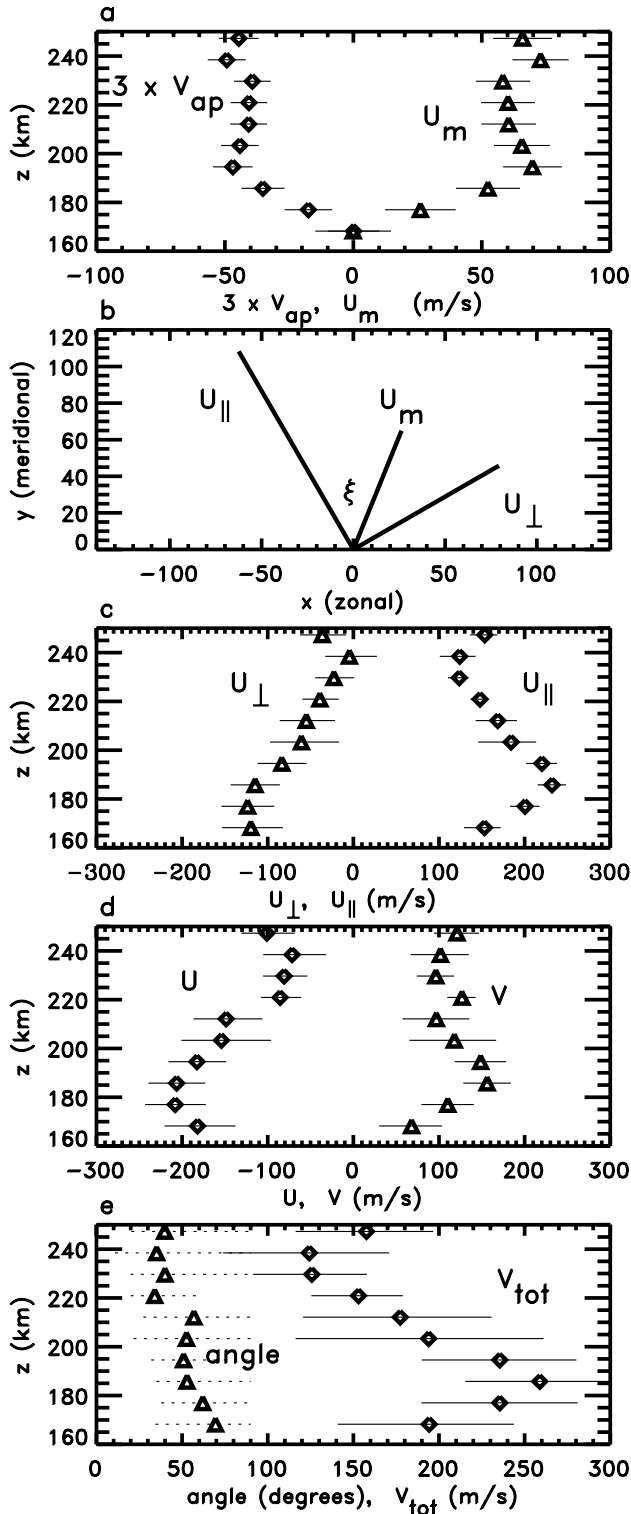


Figure 3. (a) Measured mean ion velocity, V_{ap} , multiplied by 3 (diamonds). Calculated horizontal velocity which induced V_{ap} , U_m (triangles), neglecting diffusion. (b) Orientation of U_{\perp} , U_{\parallel} and U_m . (c) Calculated values of U_{\perp} (triangles) and U_{\parallel} (diamonds). (d) Zonal (diamonds) and meridional (triangles) components of the total, background, neutral wind. (e) Total neutral wind, V_{tot} (diamonds), and angle of V_{tot} counterclockwise from north (triangles). Errors are shown as solid, horizontal lines. Errors in the angle in Figure 3e are shown as dotted lines.

We define $U_{\parallel} = -U_H$ to be in the positive wind direction. As depicted in Figure 3b, U_m and U_{\parallel} are 2 independent projections of the neutral wind along 2 different directions in the horizontal plane. Using simple geometry, the component of the wind perpendicular to U_{\parallel} is

$$U_{\perp} = (U_m - U_{\parallel} \cos \xi) / \sin \xi, \quad (6)$$

where ξ is the angle between U_{\parallel} and U_m . The angle of U_{\parallel} from north is $\Phi = 90 + \theta$, so $\xi \sim 22^\circ + \Phi$. U_{\perp} and U_{\parallel} are shown in Figure 3c.

[16] The zonal (eastward) and meridional (northward) neutral wind components in geographic coordinates are

$$U = U_{\perp} \cos(\Phi) - U_{\parallel} \sin(\Phi) \quad (7)$$

$$V = U_{\parallel} \cos(\Phi) + U_{\perp} \sin(\Phi). \quad (8)$$

U and V are shown in Figure 3d. The total, average, neutral wind amplitude, $V_{tot} = \sqrt{U^2 + V^2}$, is shown in Figure 3e, along with the angle of V_{tot} counterclockwise from north, $\cos^{-1}(U/V_{tot}) - 90$. Although $V_{tot} \sim 150$ m/s at $z \geq 220$ km, V_{tot} rapidly increases and decreases between $z \sim 160$ – 220 km, peaking at $z \sim 180$ km with an amplitude of 250 m/s. The direction of V_{tot} at $z \sim 220$ km is $\sim 40^\circ$ west of north, which is $\sim 10^\circ$ east of U_{\parallel} ; thus, this GW was propagating nearly opposite to the background, neutral wind. This is expected in the F region, since GWs propagating against the wind have larger ω_{gr} and λ_z than GWs propagating with or perpendicular to the wind, thereby penetrating to much higher altitudes before dissipating [Vadas and Fritts, 2006].

7. Discussion and Conclusions

[17] In this paper, we studied a GW observed by the PFISR on December 13, 2006, at 22–23:30 UT. $|\lambda_z|$ increased from $|\lambda_z| \sim 150$ km at $z \sim 160$ km to $|\lambda_z| \sim 400$ km at $z \sim 190$ km, then decreased to $|\lambda_z| \sim 200$ km at $z \sim 220$ km. Using a dissipative, GW anelastic dispersion relation, we calculated the GW's intrinsic period, $\tau_{tr}(z)$. We then calculated the projection of the neutral, background, horizontal wind along the GW propagation direction, $U_H(z)$, from $z \sim 160$ – 240 km. We found that the calculated winds at $z \sim 160$ km and $z \geq 220$ km are consistent with tidal amplitudes, but are much larger at $z \sim 180$ – 190 km: $U_H \sim -250$ m/s. We also used the mean component of the anti-parallel ion velocity, V_{ap} , to calculate the neutral wind along the magnetic meridian, U_m . We then demonstrated that the total, horizontal neutral background wind from $z \sim 160$ – 240 km can be calculated from U_H and U_m using simple geometry. However, U_m may be inaccurate here because 1) we neglected diffusion, which can be quite important, and 2) V_{los} may be biased at the lower altitudes because of the range-smearing effects of the long pulse used for these measurements. Future PFISR experiments with better range resolution in this altitude regime may rectify this second difficulty. Additionally, if two or more GWs are observed simultaneously by PFISR and propagate in different directions, U_H can be calculated separately for each GW using

GW dissipative theory, so the zonal and meridional winds can be computed via simple geometry without utilizing V_{ap} .

[18] Although we only analyzed a single GW, we demonstrated that this technique can be used to infer the average, background, horizontal neutral wind. Neutral winds are currently impossible to measure throughout the F region. Ground-based F region neutral winds are typically measured using Fabry-Perot interferometers during the nighttime, which are sensitive to the Doppler shift of an integrated emission layer and thus cannot measure vertical wind profiles. ISR-measured velocities can only infer the neutral wind component along the magnetic meridian as discussed in Section 6. Global Circulation Models predict that these thermospheric, neutral winds arise from semidiurnal and diurnal tides [e.g., Roble, 1995]. However, the accuracy of the phases and amplitudes of these model winds is uncertain.

[19] Application of this neutral wind extraction technique may allow for a deeper understanding of the neutral and plasma dynamics of the thermosphere. First, applying this technique over several days at PFISR could be used to determine the phases and amplitudes of semidiurnal and diurnal tides. Work is currently under way to determine the feasibility of extracting neutral winds on a near-continual or routine basis. Second, it could be used to verify the existence of spatially and temporally-localized neutral wind accelerations, which have been predicted to occur when GWs dissipate in the thermosphere [Vadas and Fritts, 2006]. Work is currently under way to compute the temporal variability of the extracted neutral winds. Finally, this technique could be used to observe the neutral responses to geomagnetic storms.

[20] **Acknowledgments.** SLV would like to thank D. C. Fritts and A. Richmond for helpful discussions, and MJN would like to thank Craig Heinselman for guidance. This research was supported by NSF grant ATM-0537311 and NASA contract NNH07CC81C. The data collection and analysis for PFISR was supported under NSF cooperative agreement ATM-0608577.

References

- Aponte, N., M. J. Nicolls, S. A. González, M. P. Sulzer, M. C. Kelley, E. Robles, and C. A. Tepley (2005), Instantaneous electric field measurements and derived neutral winds at Arecibo, *Geophys. Res. Lett.*, *32*, L12107, doi:10.1029/2005GL022609.
- Buonsanto, M. J., and O. G. Witasse (1999), An updated climatology of thermospheric neutral winds and F region ion drifts above Millstone Hill, *J. Geophys. Res.*, *104*, 24,675–24,687.
- Djuth, F. T., M. P. Sulzer, J. H. Elder, and V. B. Wickwar (1997), High-resolution studies of atmosphere-ionosphere coupling at Arecibo Observatory, Puerto Rico, *Radio Sci.*, *32*, 2321–2344.
- Hedin, A. E. (1991), Extension of the MSIS thermosphere model into the middle and lower atmosphere, *J. Geophys. Res.*, *96*, 1159–1172.
- Hines, C. O. (1968), An effect of molecular dissipation in upper atmospheric gravity waves, *J. Atmos. Terr. Phys.*, *30*, 845–849.
- Hines, C. O., and W. H. Hooke (1970), Discussion of ionization effects on the propagation of acoustic-gravity waves in the ionosphere, *J. Geophys. Res.*, *75*, 2563–2568.
- Hocke, K., and K. Schlegel (1996), A review of atmospheric gravity waves and traveling ionospheric disturbances: 1982–1995, *Ann. Geophys.*, *14*, 917–940.
- Nicolls, M. J., and C. J. Heinselman (2007), Three-dimensional measurements of traveling ionospheric disturbances with the Poker Flat Incoherent Scatter Radar, *Geophys. Res. Lett.*, *34*, L21104, doi:10.1029/2007GL031506.
- Pitteway, M. L. V., and C. O. Hines (1963), The viscous damping of atmospheric gravity waves, *Can. J. Phys.*, *41*, 1935–1948.
- Roble, R. G. (1995), Energetics of the mesosphere and thermosphere, in *The Upper Mesosphere and Lower Thermosphere: A Review of Experiment and Theory*, *Geophys. Monogr. Ser.*, vol. 87, edited by R. M. Johnson and T. L. Killeen, pp. 1–21, AGU, Washington, D. C.
- Thome, G. D. (1964), Incoherent scatter observations of travelling ionospheric disturbances, *J. Geophys. Res.*, *69*, 4047–4049.
- Vadas, S. L., and D. C. Fritts (2005), Thermospheric responses to gravity waves: Influences of increasing viscosity and thermal diffusivity, *J. Geophys. Res.*, *110*, D15103, doi:10.1029/2004JD005574.
- Vadas, S. L., and D. C. Fritts (2006), Influence of solar variability on gravity wave structure and dissipation in the thermosphere from tropospheric convection, *J. Geophys. Res.*, *111*, A10S12, doi:10.1029/2005JA011510.
- Vadas, S. L. (2007), Horizontal and vertical propagation and dissipation of gravity waves in the thermosphere from lower atmospheric and thermospheric sources, *J. Geophys. Res.*, *112*, A06305, doi:10.1029/2006JA011845.
- M. J. Nicolls, Center for Geospace Studies, SRI International, Menlo Park, CA, USA. (michael.nicolls@sri.com)
- S. L. Vadas, CoRA Division, NWRA, 3380 Mitchell Lane, Boulder, CO 80301, USA. (vasha@cora.nwra.com)